Energy & Environmental Science

RSC Publishing

PAPER

Bi-hierarchical nanostructures of donor–acceptor copolymer and fullerene for high efficient bulk heterojunction solar cells†

Cite this: *Energy Environ. Sci.*, 2013, **6**, 1938

Hsueh-Chung Liao,[a] Cheng-Si Tsao,*[b] Yu-Tsun Shao,[c] Sheng-Yung Chang,[c] Yu-Ching Huang,[b] Chih-Min Chuang,[b] Tsung-Han Lin,[a] Charn-Ying Chen,[b] Chun-Jen Su,[d] U-Ser Jeng,[d] Yang-Fang Chen[c] and Wei-Fang Su*[a]

Received 10th December 2012
Accepted 2nd April 2013

DOI: 10.1039/c3ee24312e

www.rsc.org/ees

Solvent additive processing has become the most effective method to tune the nanostructure of donor–acceptor (D–A) type copolymer/fullerene bulk heterojunctions (BHJs) solar cells for improving power conversion efficiencies. However, to date qualitative microscopic observations reveal discrepant results on the effects of solvent additives. Here, we present quantitative evolution of bi-hierarchical nanostructure of D–A copolymers and fullerenes by employing grazing-incidence small/wide angle X-ray scattering (GISAXS/GIWAXS) techniques and [2,6-(4,4-bis(2-ethylhexyl)-4*H*-cyclopenta[2,1-*b*;3,4-*b*′]-dithiophene)-*alt*-4,7-(2,1,3-benzothiadiazole)]/[6,6]-phenyl-*C*71-butyric acid methyl ester (PCPDTBT/PCBM) BHJ as model materials. An accurate GISAXS model analysis is established herein for revealing the distinctive bi-hierarchical nanostructures from molecular level to a scale of hundreds of nanometers. The mechanisms of hierarchical formation and mutual influence between PCPDTBT and PCBM domains are proposed to correlate with photovoltaic properties. These results provide a comprehensive interpretation in respect to previous studies on the nanostructures of D–A copolymer/fullerene BHJs. It is helpful for optimum structural design and associated synthesis improvement for achieving high efficiency BHJ solar cells.

Broader context

Polymer photovoltaics have achieved high power conversion efficiency toward commercial validity. The processing with solvent additives has been the most widely used strategy to control and optimize the nanomorphology of donor–acceptor type copolymer/fullerene bulk heterojunctions (BHJs). However, the effects and mechanisms of solvent additives are still unclear to date based on the discrepant reported results of various polymer/fullerene BHJs. The present work employed gracing incidence small/wide angle scattering (GISAXS/GIWAXS) to thoroughly and quantitatively resolve the nanostructure of PCPDTBT/$PC_{71}BM$ BHJs. An accurate structural model is established herein which reveals bi-hierarchical nanostructures of polymer and PCBM in different length scales. The additive-tuned structural evolution is characterized which enables an in-depth understanding of the film forming mechanism in a kinetic point of view and the mutual interaction among polymer, PCBM, additive and host solvent molecules. The results reasonably interpret the different microscopic studies on the additive effect and the rationally optimized processing parameters of various copolymer/PCBM bulk heterojunction solar cells. This work demonstrates a comprehensive characterization and successfully extends the results to a general and broad concept of different materials systems.

[a]*Department of Materials Science and Engineering, National Taiwan University, No. 1, Sec. 4, Roosevelt Road, Taipei 10617, Taiwan. E-mail: suwf@ntu.edu.tw; Fax: +886 2 33664078; Tel: +886 2 33664078*

[b]*Institute of Nuclear Energy Research, No. 1000, Wenhua Road, Longtan Township, Taoyuan County 32546, Taiwan. E-mail: cstsao@iner.gov.tw; Tel: +886 3 4711400 ext. 3420*

[c]*Department of Physics, National Taiwan University, No. 1, Sec. 4, Roosevelt Road, Taipei 10617, Taiwan*

[d]*National Synchrotron Radiation Research Center, No. 101, Hsin-An Road, Hsinchu 300-77, Taiwan*

† Electronic supplementary information (ESI) available: Representative 2D GISAXS, 2D GIWAXS patterns and the integration of GIWAXS patterns. The background effect and PEDOT:PSS effect on the GISAXS profiles and the resolved nanostructures of the sample films. Estimation of the $\Delta\rho$ value in model fitting. Discussion of the polymer morphology. Cross examination of model fitting of PCPDTBT/PCBM (78% PCBM) films processed with x% DIO ($x \geq 3$). Scattering intensities calculated by various terms of SAXS models. Scheme of additive effect based on different D–A copolymer systems. Discussion and scheme of the interaction among additive molecules, PCBM and polymer during solvent evaporation. Correlation of nanostructures to optoelectronic and photovoltaic properties regarding absorption spectrum, photocurrent–voltage characteristics, and carrier mobility of PCPDTBT/PCBM blend films. Pictures of BL78_10% DIO film as-casted and stored in glove box for one day respectively. See DOI: 10.1039/c3ee24312e

1 Introduction

Bulk heterojunction (BHJ) solar cells adopting new donor–acceptor (D–A) conjugated copolymers has achieved high power conversion efficiency (PCE) of 7–8%.[1–5] Controlling the nanoscale morphology of bi-continuous interpenetrating networks of phase-separated polymer (donor) and fullerene (acceptor) domains is an extremely critical step to improve device performances. The solvent additive-processed approach has shown to be the most effective method to manipulate the BHJ nanostructure and has been extensively investigated.[1–3,6–12] However, the reported microscopic observations of the additive effect are quite different based on different D–A copolymer/fullerene BHJs. Heeger's group demonstrated that the fullerene-rich domains in the PCPDTBT/PCBM BHJ film processed with solvent additives become much larger than that without.[8,9] On the contrary, the other TEM observations show that processing additives can disperse large PCBM-rich domains to much smaller PCBM clusters.[3,10,11] Similar phenomenon of suppressing large-scale PCBM aggregation due to solvent additives was also found in the PTB7/PCBM BHJ studied by small-angle X-ray scattering (SAXS) in the solution phase.[12] Therefore, a thoroughly and quantitatively structural characterization of BHJ films regarding the polymer crystallization, fullerene aggregation and their mutual influence at multiple-length-scales and correlation to optoelectronic properties is necessary.

Comprehensive reviews of the nanostructural characterization can be found in ref. 13 and 14. GISAXS/GIWAXS technique has shown to be a powerful tool in structural characterization of BHJ blend films.[6,7,11,15–21] However, the current GISAXS investigation of PCBM phase structure in D–A copolymer/fullerene BHJs is still few.[15,16] PCPDTBT polymer as a potential model material of D–A type copolymer is frequently investigated.[6,7,15] In this work, we employed GISAXS and GIWAXS to systematically investigate the hierarchical structures of both PCPDTBT and PCBM aggregated domains and networks respectively (*i.e.* bi-hierarchical nanostructures from molecular level to various length (nm) scales tuned by different amounts of additive, 1,8-diiodooctane (DIO) and PCBM contents respectively). One of the characteristic length scales of aggregated PCPDTBT crystals is comparable to that of PCBM aggregation clusters. Namely, in the present quantitatively multi-length-scale GISAXS analysis, we resolved the comparable morphological structures that are contributed by crystalline polymer PCPDTBT and PCBM aggregations, respectively, relative to the surrounding amorphous polymer/PCBM molecules matrix. The GISAXS characterizations are distinctly different from the past studies of P3HT/$PC_{61}BM$ systems of which only nanoscale $PC_{61}BM$ clusters contributed to the GISAXS intensities relative to large-scale amorphous polymer domains.[18–20] The SAXS analysis model in the present case is a challenge and has been accurately established herein. It quantitatively provides an insight into the structural BHJ model and bi-hierarchical structural evolution of both fractal-network-aggregated polymer crystals and fractal-structure fullerene clusters. The other microscopic techniques including TEM, atomic force microscope (AFM) and Kelvin probe force microscope (KPFM) were complementally conducted to further evidence the resolved nanomorphology. The mechanism of bi-hierarchical formation and mutual influence between PCPDTBT and PCBM mediated by different additive contents and PCBM amounts can be rationally proposed. It can reasonably interpret the discrepancy among the reported literatures[3,8–12,15] and be extended to other D–A type copolymers and other fullerene derivatives.[17,18,22,23] The test of corresponding devices were finally performed to understand the relationship between three-dimensional bi-hierarchical structure, OPV properties and performance regarding light harvesting, exciton dissociation and charge transport.

2 Experimental section

The pristine PCPDTBT films were spin coated using the PCPDTBT (1-Materials, $M_w \sim 35\,000$, PDI ~ 2.5) solution (10 mg ml^{-1}) in chlorobenzene (Acros, 99%) and different volume fractions of solvent additive DIO (Aldrich, 98%) respectively. They are denoted as P_w/o DIO, P_0.5% DIO, P_3% DIO, P_5% DIO, and P_10% DIO respectively. The BHJ thin films processed with different amounts of DIO were obtained from blending solutions of PCPDTBT (10 mg ml^{-1}) and PCBM (Solenne B.V. Inc., >99%, 36 mg ml^{-1}), *i.e.* 78 wt% loading ratio of PCBM, and are denoted as BL78_w/o DIO, BL78_0.5% DIO, BL78_3% DIO, BL78_5% DIO and BL78%_10% DIO respectively. The BHJ thin films with different loading amount of PCBM were also prepared by blending PCPDTBT (10 mg ml^{-1}) with PCBM 5 mg ml^{-1}, 10 mg ml^{-1}, 36 mg ml^{-1} respectively in chlorobenzene and 3% DIO solvent. These BHJ films are denoted as BL33_3% DIO, BL50_3% DIO, and BL78_3% DIO respectively.

For solar cell device fabrication, the transparent electrode indium tin oxide (ITO) coated substrate was first ultrasonically cleaned by a series of solvents, *i.e.* ammonia/H_2O_2/DI water, methanol, isopropanol and subsequently treated by oxygen plasma. A 30 nm hole transporting layer poly(3,4-ethylenedioxythiophene) poly(styrenesulfonate) (PEDOT:PSS, Baytron P 4083) was spin coated on the substrate and baked at 130 °C for 15 min. Afterwards, the substrates were transferred to the glove box and the BHJ layers were deposited respectively from the prepared PCPDTBT/PCBM solutions. Finally, the top electrode Ca/Al with thickness of Ca: 40 nm and Al: 120 nm were deposited by thermal evaporation in 2×10^{-6} Torr vacuum chamber to complete the photovoltaic devices with area of 0.06 cm^2. It is noteworthy that the film morphology would evolve after the spin coating process with the gradually evaporated DIO solvent because of it high vapor pressure. Therefore, for both the device fabrication and film sample preparation for morphological characterization, the PCPDTBT films and the PCPDTBT/PCBM blend films were spin coated and placed in a glove box overnight in order to ensure the thin films attaining a steady morphology. Subsequently, for completely removing the residue DIO, the devices and the film samples were dried by being kept in a vacuum chamber for at least one day prior to use. According to ref. 15 it can ensure the complete removal of the additive. The electron mobility and hole mobility of the BHJ films were measured by modeling the current–voltage curves of

electron-only and hole-only device respectively, *i.e.* electron: Al/BHJ films/Al, hole: ITO/PEDOT:PSS/BHJ films/Au using field-dependent space carrier limited current (SCLC) method. The current–voltage curves of both PCE and SCLC were recorded by Keithley 2400 source meter and performed in air. The photocurrent of photovoltaic devices was characterized under A.M. 1.5 radiation (100 mW cm^{-2}) of a solar simulator source (Newport Inc.).

The GIWAXS results were carried out at beam line 17A of National Synchrotron Radiation Research Center (NSRRC), Taiwan, with the incidence angle of 0.2°. Note that the reported GIWAXS profiles are taken along the Q_z direction defined similarly as that for X-ray power diffraction (of a constant incident angle), rather than the Q_z definition in the crystallography diffraction (with θ–2θ scans).[24] All the GIWAXS profiles presented in this study were carefully calibrated in the scattering wave vector, Q_z and Q_x, using standard samples made of Ag-behenate. The characteristic peaks measured for a film of Ag-behenate in GIWAXS mode (in the same sample geometry) overlap reasonably well with that in the X-ray powder scattering pattern measured for the standard sample of a powder form, within ±0.5% accuracy in Q_z. It implies that the reported Q_z values for the GIWAXS profiles, hence the *d*-spacing of the polymer crystallites, are at least within this accuracy. On the other hand, the systematic difference in Q_z definition should not affect the comparisons of the relative peak position and integrated intensity of the (100) peaks of the samples and the conclusions made accordingly.

The GISAXS measurement was performed at beam line 23A of NSRRC, Taiwan. The detailed experimental setup can found elsewhere.[17,18] Two instrumental configurations were used to obtain a different *Q*-range. In short, the thin films were directly deposited on 2 cm × 1 cm silicon wafer and dried in vacuum for at least one day prior to use. Afterwards, they were characterized by a monochromated X-ray beam (8 keV, wavelength λ = 1.55 Å, incidence angle = 0.2°). The two dimensional scattering patterns were collected by a CCD detector (MAR165, 165 mm in diameter, 1024 by 1024 pixels resolution) that is situated 312 cm and 515 cm from the samples in order to obtain two different *Q*-range respectively. The 1-D GISAXS profiles were reduced by integrating the 2-D patterns along the in-plane direction, *i.e.* $Q_Z = 2\pi\lambda^{-1}(\sin\alpha_i + \sin\alpha_f)$ with α_i, ϑ and α_f being the incident, in-plane, and out-of-plane scattering angles of X-ray. The reduced 1-D GISAXS profiles obtained from the two experimental configurations were merged together. The TEM images were obtained from FEI Tecnai G2 T20 microscope operating at 200 KeV. The UV-visible spectrometer (PerkinElmer Lambda 35) was utilized to obtain the ultraviolet-visible absorption spectra of the thin films. For the surface topography and surface potential mapping carried out by KPFM (Digital Instruments, Nanoscopes III), a conductive tip with resonance frequencies of 75 kHz in average and coated with platinum–iridium alloy was used to scan in tapping mode. After acquiring the topographic profile along the scanning line, the tip was lifted accordingly by 20 nm and rescanned to detect the surface potential which ensures the elimination of topography effect.

3 Results and discussion

3.1 Morphologies of pristine PCPDTBT films affected by processing additive

The pristine PCPDTBT films without and with 0.5%, 3%, 5% and 10% (in volume) of DIO were prepared and denoted as P_w/o DIO, P_0.5% DIO, P_3% DIO, P_5% DIO and P_10% DIO, respectively. The synchrotron X-ray source was used for the GISAXS/GIWAXS experiments herein.[25] The 1D GISAXS profiles reduced along the in-plane direction (*i.e.*, parallel to substrate) of these films are expressed as a function of scattering vector Q_X (Fig. 1a). The corresponding 1D GIWAXS profiles reduced along out-of-plane direction (normal to substrate) are selectively shown in Fig. 1b as a function of scattering vector Q_Z. The representative 2D GISAXS and GIWAXS patterns are shown in the ESI, Fig. S1.† Note that all the GISAXS/GIWAXS experiments were performed by using the silicon as a substrate with the film sample deposited on top. The effects of background subtraction and existing of poly(3,4-ethylenedioxythiophene) poly(styrenesulfonate) (PEDOT:PSS) layer on the substrates are detailed in the ESI, Fig. S3–S5.† The GIWAXS profiles reveals the lamellar spacing and partial crystallinity contributed by edge-on polymer crystals with (100) lamellar layers oriented parallel to the substrate. The domain size of polymer crystallites *L* and the corresponding (100) lamellar spacing *l* calculated from the full-width at half maximum (FWHM) values ΔQ ($L = 2\pi/\Delta Q$) and the position of (100) peaks ($l = 2\pi/Q$) respectively are found to be L = 5–7 nm and $l \sim 1.2$ nm which are consistent with the other studies.[6,7]

An in-plane GISAXS profile of a pristine P3HT film with similar thickness was also measured for comparison (Fig. 1a). The GISAXS intensity profile of the P3HT film scales as Q^{-4}. It can be model-fitted by the Debye–Bueche Equation (also called Debye–Anderson–Brumberger, DAB, model),[26] signifying a mesoscale domain of P3HT amorphous chains.[18,19] Zhang *et al.* reported the observed shoulder in the GISAXS profiles of P3HT and attributed to the fibril formation of P3HT crystallites.[27] However, in the present work the P3HT had a molecular weight of 60 kDa which is not expected to form fibril like crystallites.[28] Therefore, the GISAXS contributed by P3HT crystalline domain (~20 nm in size[18,19]) can be neglected here due to the lack of obvious form factor profile (Fig. 1a). Unlike the P3HT film, the in-plane GISAXS profile of the pristine PCPDTBT film (P_w/o DIO) shows a shoulder (or a little peak) in the middle-*Q* region (0.01–0.03 $Å^{-1}$) following an upturn in the low-*Q* region (<0.01 $Å^{-1}$) with a power-law behavior of fractal dimension *D* ($I(Q) \propto Q^{-D}$; 1 ≤ exponent D ≤ 3). The GISAXS profile of the PCPDTBT film processed with 0.5% of DIO has a much higher intensity and a remarkable shoulder. The shoulder shape of these profiles can be regarded as the intensities contributed mainly by the form factor scattering of primary crystalline particles and little structural factor (inter-particle effect). This fractal system is formed by the aggregation of primary particles. Generally, the fractal system is a characteristic of self-similar geometry. It can be characterized by SAXS technique. The power-law dependence of scattering intensity in the low-*Q* region is related to the quantity of fractal dimension which

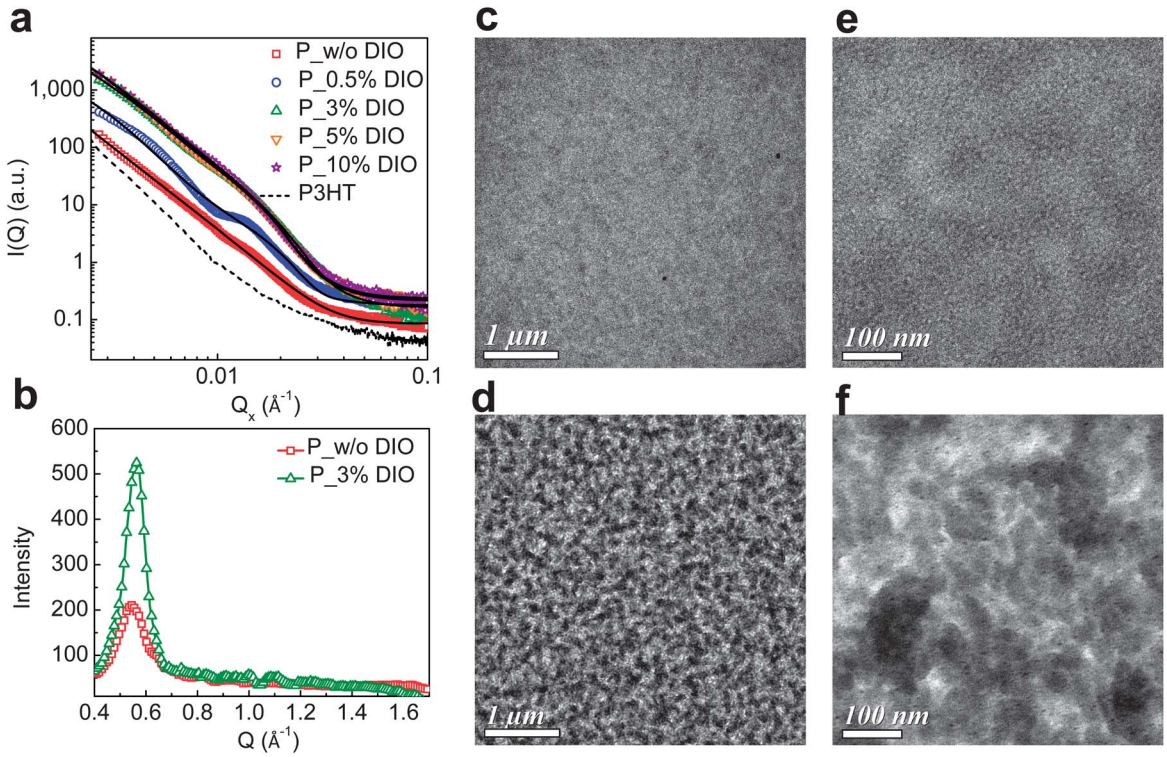

Fig. 1 (a) GISAXS profiles of pristine PCPDTBT thin films processed without and with 0.5%, 3%, 5%, 10% DIO, *i.e.* P_w/o DIO, P_0.5% DIO, P_3% DIO, P_5% DIO and P_10% DIO respectively. The GISAXS profile of pristine P3HT is also shown as the black dash line. The solid lines represent the model-fitted intensities. (b) GIWAXS profiles of pristine PCPDTBT processed without and with 3% DIO, *i.e.* P_w/o DIO and P_3% DIO respectively. (c, d, e and f) TEM images of pristine PCPDTBT films processed without (c and e) and with 3% DIO (d and f) respectively. The spherical-like domains in (f) represent the PCPDTBT aggregated crystallites, *i.e.* PCPDTBT primary particles that comprise several PCPDTBT basic crystallites.

reveals an openness, branch or dense characteristics of complicate structures of aggregation. Moreover, the GISAXS intensities of PCPDTBT films processed with 3%, 5% and 10% DIO largely increase, especially the power-law scattering in the low-Q region. It signifies that the degree of fractal aggregation is substantially enhanced. Fig. 1a shows that the effect of DIO amount on the morphology of aggregated polymer crystals achieves a saturation behavior higher than 3% of DIO.

A GISAXS study of low band-gap polymer/PCBM blends processed with additive reported that the main PCBM phase is formed by fractal-like aggregations.[13] The fractal-like aggregation formed by PCPDTBT polymer crystallites and the related GISAXS analysis are reported here for the first time. The scattering intensity of PCPDTBT films can be expressed as:

$$I_f(Q) = P(Q)\, S(Q) + b \qquad (1)$$

where $P(Q)$ is related to the form factor of primary particles (approximated by spherical shape of radius R here), and $S(Q)$ is the fractal structure factor, describing the interaction between primary particles in this fractal-like aggregation system. The constant b is due to incoherent scattering background. $P(Q)$ includes the product of particle volume fraction φ, the square of scattering length density difference between crystalline and amorphous polymers $\Delta\rho^2$ and crystalline particle volume V_P. $S(Q)$ is given by[29]

$$S(Q) = 1 + \frac{\sin[(D-1)\tan^{-1}(Q\xi)]}{(QR)^D} \frac{D\Gamma(D-1)}{\left[1+1/(Q\xi)^2\right]^{(D-1)/2}} \qquad (2)$$

where ξ is the correlation length of the fractal-like network (or domain) formed by the aggregation of primary particles. D is the fractal dimension. R is the mean radius of primary particles. The domain size of this network or domain is approximately characterized by R_g, where R_g is the Guinier radius of this fractal-like network and $R_g = [D(D+1)/2]^{1/2}\xi$.[30] Eqn (1) can be modified by taking into account the polydispersity of primary particles having a Schulz distribution. The polydispersity of size distribution is p. The GISAXS profiles of the pristine PCPDTBT films processed without and with different amounts of DIO can be fitted well using the fractal model of polydispersed primary particles, as shown in Fig. 1a (except for the case of 0.5% of DIO due to the inter-particle effect on the shoulder region). The structural parameters of $\varphi_{PCPDTBT}$, $2R_{PCPDTBT}$, $D_{PCPDTBT}$, $\xi_{PCPDTBT}$ and $R_{g\text{-}PCPDTBT}$ determined by the model fitting are summarized in Table 1. The estimation of scattering length density (SLD) difference ($\Delta\rho$; scattering contrast) between the particles and the surrounding matrix during model fitting is detailed in the ESI (Table S1†).

According to Table 1, the relative volume fraction of polymer crystallites in the PCPDTBT film processed without DIO is the lowest as compared to those of the other films processed with

Table 1 Structure parameters of pristine PCPDTBT film processed without and with 0.5%, 3%, 5%, 10% DIO, *i.e.* P_w/o DIO, P_0.5% DIO, P_3% DIO, P_5% DIO and P_10% DIO respectively

Thin film	$\varphi_{PCPDTBT}$ (%)	$2R_{PCPDTBT}$ (nm)	$\xi_{PCPDTBT}$ (nm)	$D_{PCPDTBT}$	$R_{g\text{-}PCPDTBT}$ (nm)
P_w/o DIO	1.3	7	109	2.5	251
P_3% DIO	19.7	20	60	~3	146
P_5% DIO	21.0	20	60	~3	146
P_10% DIO	21.6	20	61	~3	149

DIO. The size of the primary particle ($2R_{PCPDTBT} \sim 7$ nm) is close to that of polymer crystallite determined by GIWAXS (defined as basic crystallite here). The fractal dimension D of aggregation by the basic crystallite is 2.5, suggesting a loose and open structure. The corresponding TEM observations are shown in Fig. 1c and e which consistently reveal the disperse-like aggregation domains with poor contrast. However, the relative volume fraction of polymer crystallites in the DIO-processed PCPDTBT films increases with the amount of additive and saturates at 3% DIO. In the cases (DIO $\geq$ 3%), the primary particle is $2R_{PCPDTBT} \sim 20$ nm in size which comprises aggregation of several basic crystallites. The primary particles then aggregate to form the fractal-like domains. Their fractal dimensions are close to 3.0 which signify a dense structure in the aggregated domains. Interestingly, the TEM observation in Fig. 1d (low magnification) shows the short fibril-like morphology of polymer, which is similar to that demonstrated by the other group of the PCPDTBT/PCBM blend films (Fig. 5 of ref. 9). However, Fig. 1f (high magnification) clearly shows the fractal-like structure comprising spherical-like domains which is consistent with the GISAXS modeling results. This observation is similar to the image of which the PCBM was removed by chemical treatment (Fig. 6 of ref. 9). Actually, the reported morphology of the D–A copolymer is different based on the microscopic observations. We have a detailed discussion in the ESI (Fig. S6†) of the D–A copolymer morphology as compared to conventional polymer P3HT. Based on the accurate SAXS modeling, we conclude the proposed model herein (fractal-like aggregation of network from basic crystallites) is a reasonable structural model to describe the distinctive structure of PCPDTBT polymer crystals in hierarchical structures. This comprises (1) basic crystallite ($L \sim 5$ nm), (2) primary particles ($2R_{PCPDTBT} \sim 20$ nm) aggregated by basic crystallites and (3) fractal-like-network domain ($R_{g\text{-}PCPDTBT} \sim 150$ nm) aggregated by primary particles. In contrast to the polymer crystals, the other part is amorphous polymer chains having large domains as the surrounding matrix.

3.2 Morphologies of PCPDTBT/PCBM blends affected by processing additive

For the PCPDTBT/PCBM blend films, we first investigated the 78% (in weight) PCBM content because it can allow for the best PCE as compared to other PCBM contents (discuss later). Note that the PCBM herein is the abbreviation of $PC_{71}BM$ which is generally used for achieving high PCE. The PCPDTBT/PCBM blend films processed without and with 0.5%, 3%, 5% and 10% of DIO are denoted as BL78_w/o DIO, BL78_0.5% DIO, BL78_3% DIO, BL78_5% DIO and BL78_10% DIO, respectively. The reduced in-plane GISAXS and out-of-plane GIWAXS of these blend films are shown in Fig. 2a and b, respectively. The GISAXS profiles of BL78_w/o DIO and BL78_0.5% DIO blend films show the same profiles with the lowest intensity and without any obvious shoulder in the middle-Q region in comparison to that of pristine polymer (Fig. 1a) films and the other blend films (BL78_x% DIO, $x \geq 3$). It reveals that the incorporation of PCBM disrupts the formation of PCPDTBT polymer crystal when the amount of DIO is less than 0.5%. The corresponding GIWAXS profiles (Fig. 2b) consistently show that no scattering peak (*i.e.*, almost no polymer crystallization) of BL78_w/o DIO and BL78_0/5% DIO films. Therefore, The GISAXS intensities of these two films can be regarded as (1) the scattering purely from PCBM-rich phase and (2) PCPDTBT amorphous polymer chains. This system can be modeled as follows:

$$I(Q) = I_{D\text{–}B}(Q) + I_F(Q) + b \quad (3)$$

where $I_{D\text{–}B}(Q)$ is the intensity model by the Debye–Bueche equation ($\propto Q^{-4}$) which describes a large molecular PCBM/amorphous PCPDTBT domain.[18] $I_F(Q)$ mainly in $Q < 0.02$ Å^{-1} is used to characterize the structure of PCBM-rich phase assuming the fractal-like aggregation (eqn (1)). Namely, the PCBM molecules ($2R_{PCBM} \sim 1$ nm) as the primary particles aggregate to form fractal-like clusters. The GISAXS profiles of BL78_w/o DIO and BL78_0.5% DIO blend films can be fitted well using the model of eqn (3) (solid lines in Fig. 2a). Similarly the domain size ($R_{g\text{-}PCBM}$) of fractal-like aggregation is obtained according to $R_{g\text{-}PCBM} = [D_{PCBM}(D_{PCBM} + 1)/2]^{1/2}\xi_{PCBM}$. The structural parameters of φ_{PCBM}, D_{PCBM}, ξ_{PCBM} and $R_{g\text{-}PCBM}$, based on new $\Delta\rho^2$ (ESI, Table S1†) value for PCBM phase and the fixed size (1 nm) of primary particle for PCBM molecule, are listed in Table 2. Interestingly, the determined fractal dimension is very low ($D_{PCBM} \sim 1.5$), signifying a very loose (pearl-string-like) structure. Their correlation lengths ξ for fractal-like domains are relatively large (~100 nm). The GISAXS analysis suggests that PCBM molecules are dispersed in the polymer matrix but retain little aggregation. The quantitative GISAXS analysis of nanomorphology evidences the disruption of polymer crystallization by the dispersed PCBM for the blend films (containing 78% PCBM) processed without or with few amount of DIO (≤0.5%). It is also consistently revealed by GIWAXS results (Fig. 2b).

The GISAXS profiles of the BL78_3% DIO, BL78_5% DIO and BL78_10% DIO blend films show a significant increase in the scattering intensities, revealing the formation of new nanomorphology (Fig. 2a). The corresponding GIWAXS profiles show the enhanced PCPDTBT (100) scattering intensities which indicate the larger volume fractions of polymer crystal structures with increased DIO amounts (Fig. 2b). In this case, the GISAXS intensity is contributed by both aggregated polymer crystals and fullerene clusters relative to the matrix of amorphous polymer (heterogeneously mixed with PCBM molecules). How to accurately resolve these two structures using the GISAXS technique is a challenge. There are two independent approaches in the present work (see details in the

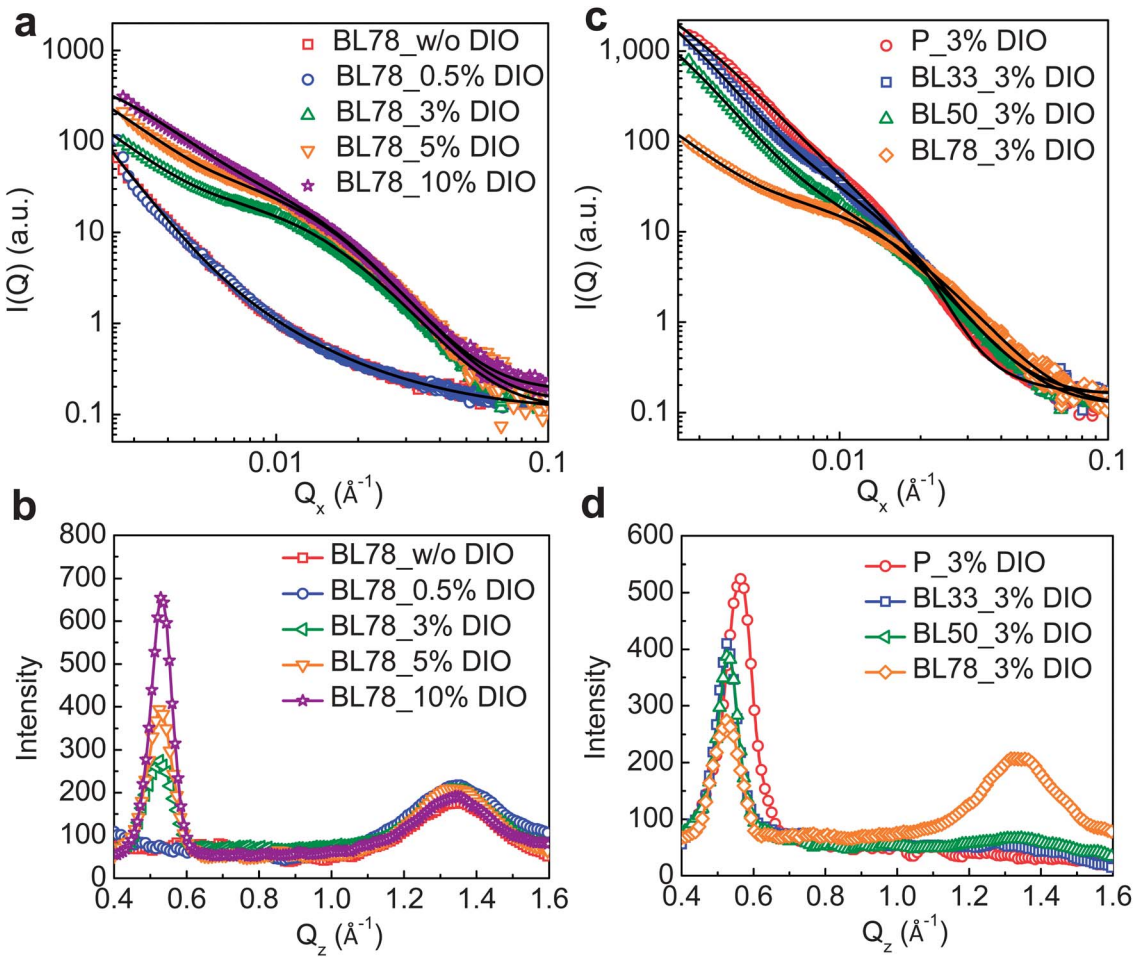

Fig. 2 (a) GISAXS and (b) GIWAXS profiles of PCPDTBT/PCBM (78 wt% PCBM) blend films processed without and with 0.5%, 3%, 5%, 10% DIO, *i.e.* BL78_w/o DIO, BL78_0.5% DIO, BL78_3% DIO, BL78_5% DIO, and BL78_10% DIO respectively. (c) GISAXS and (d) GIWAXS profiles of pristine PCPDTBT film and PCPDTBT/PCBM blend films with 33%, 50%, 78 wt% PCBM respectively. These films were processed with 3% DIO, *i.e.* P_3% DIO, BL33_3% DIO, BL50_3% DIO, and BL78_3% DIO. The solid lines in (a) and (c) represent the model-fitted intensities.

ESI, Fig. S7, Table S2†). In the first approach (I), we try to get the GISAXS intensity purely contributed by the aggregated PCBM clusters. It can be obtained by subtracting the concentration-normalized GISAXS profile (Fig. 1a) from that of the blend film processed with the same amount DIO (Fig. 2a). The shape of subtracted profiles (ESI, Fig. S7†) is characteristic of a typical fractal system and can be fitted well using the fractal aggregation model with PCBM molecules (1 nm in size) as primary particles. In the approach (II), we simultaneously modeled the structures of PCBM clusters and PCPDTBT polymer crystals in a nonlinear least-squares fitting to the GISAXS data, as given by:

Table 2 Structural parameters of PCPDTBT/PCBM blend (78% PCBM) processed without and with 0.5%, 3%, 5%, 10% DIO, *i.e.* BL78_w/o DIO, BL78_0.5% DIO, BL78_3% DIO, BL78_5% DIO, and BL78_10% DIO respectively, and different PCBM contents (33% and 50%) processed with 3% DIO, *i.e.* BL33_3% DIO and BL50_3% DIO respectively. The champion PCEs of the solar cells devices based on these thin films are also listed. The values in parentheses show the average PCEs and PCE distribution (standard deviation) obtained from 20 devices made from 10 independently prepared BHJ films

Thin film	$\varphi_{PCPDTBT}$ (%)	$\xi_{PCPDTBT}$ (nm)	$R_{g\text{-}PCPDTBT}$ (nm)	φ_{PCBM} (%)	D_{PCBM}	ξ_{PCBM} (nm)	$R_{g\text{-}PCBM}$ (nm)	PCE (%)
BL78_w/o DIO	n/a	n/a	n/a	46	1.5	100	137	3.20 (3.07 ± 0.13)
BL78_0.5% DIO	n/a	n/a	n/a	46	1.5	100	137	3.61 (3.38 ± 0.18)
BL78_3% DIO	3.2	51	125	34	~3.0	6.1	14.9	5.20 (5.00 ± 0.12)
BL78_5% DIO	3.6	46	113	37	~3.0	6.6	16.1	4.92 (4.72 ± 0.09)
BL78_10% DIO	8.2	31	91	37	~3.0	6.7	16.4	3.98 (3.68 ± 0.22)
BL33_3% DIO	12.8	44	108	13	~3.0	6.5	15.9	1.92 (1.65 ± 0.19)
BL50_3% DIO	10.6	58	142	18	~3.0	6.5	15.9	3.64 (3.47 ± 0.11)

$$I(Q) = I_{PCBM}(Q) + I_{PCPDTBT}(q) + b \quad (4)$$

where $I_{PCBM}(Q)$ (mainly in $Q < 0.02$ Å^{-1}) is the fractal aggregation model with PCBM molecules as the primary particles. $I_{PCPDTBT}(Q)$ (mainly in 0.02 Å^{-1} < Q < 0.04 Å^{-1}) is the fractal aggregation model with polydispersed PCPDTBT primary particle, as previously described. During the fitting procedure, the primary particle size of PCPDTBT is fixed at $2R_{PCPDTBT} = 20$ nm which is identical to those of pristine PCPDTBT films processed with x% DIO, $x \geq 3$. The GISAXS profiles of the BL78_3%, BL78_5% and BL78_10% DIO blend films can be fitted well using the model of eqn (4) (solid lines in Fig. 2a) and the structural parameters are summarized in Table 2. For justifying the adopted model and approach determining the PCBM structure, we independently examine the results as compared to those of approach (I) as shown in the ESI, Table S2.† The cross-check results are consistent with each other. However, there still exists the unknown uncertainty due to the model-dependent assumption. Additionally, the scattering intensities contributed by various terms of SAXS models of BL78_w/o DIO (using eqn (3)) and BL78_3% DIO (using eqn (4)) blend films as the examples are resolved to shown in the ESI, Fig. S8,† together with the resultant fitting intensities. The quantitative contributions from PCBM clusters and PCPDTBT crystalline domains can be understood to evaluate the sensitivities to the SAXS analysis model.

As compared to the values of fractal dimension $D_{PCBM} \sim 1.5$ and correlation length $\xi_{PCBM} \sim 100$ nm of nearly dispersed PCBM phase in the BL78_w/o DIO and BL78_0.5% DIO blend films, the PCBM phase of the blend films BL78_x% DIO, $x \geq 3$ ($D_{PCBM} \sim 3.0$; $\xi_{PCBM} \sim 6$–7 nm) shows a significantly dense (fractal-like) aggregation state. The relative volume fraction of large PCBM internally dispersed domain decreases from ~46% to 34–37% for the small internally dense domain. Consistently, the transition of hierarchical PCPDTBT crystallites from no crystallization of BL78_w/o DIO and BL78_0.5% DIO blend films to the fractal-like aggregation developed by primary particles of aggregated basic crystallites appears at $x \geq 3$ (DIO amount). It suggests that the relative volume fraction of the PCBM phase is significantly constrained by the increasing volume fraction of PCPDTBT crystallites. Apparently, the amount of DIO plays a role in the competition between PCBM and PCPDTBT. It is also found that the variation in both the relative volume fraction and correlation length of PCBM phase with the DIO amount (from 3 to 10%) is stable (Table 2), revealing the development and growth of PCBM cluster is confined by PCPDTBT crystal networks.

Fig. 3 shows the complementary microscopic observations including KPFM AFM and TEM of BL78_w/o% DIO and BL78_3% DIO films respectively. It is noteworthy that AFM analysis can only provide the topographic morphology of a thin film. The KPFM measurement of which the contrasts are resulted from the work function difference between the donor and acceptor components can powerfully identify the material distributions. The KPFM surface potential mapping was

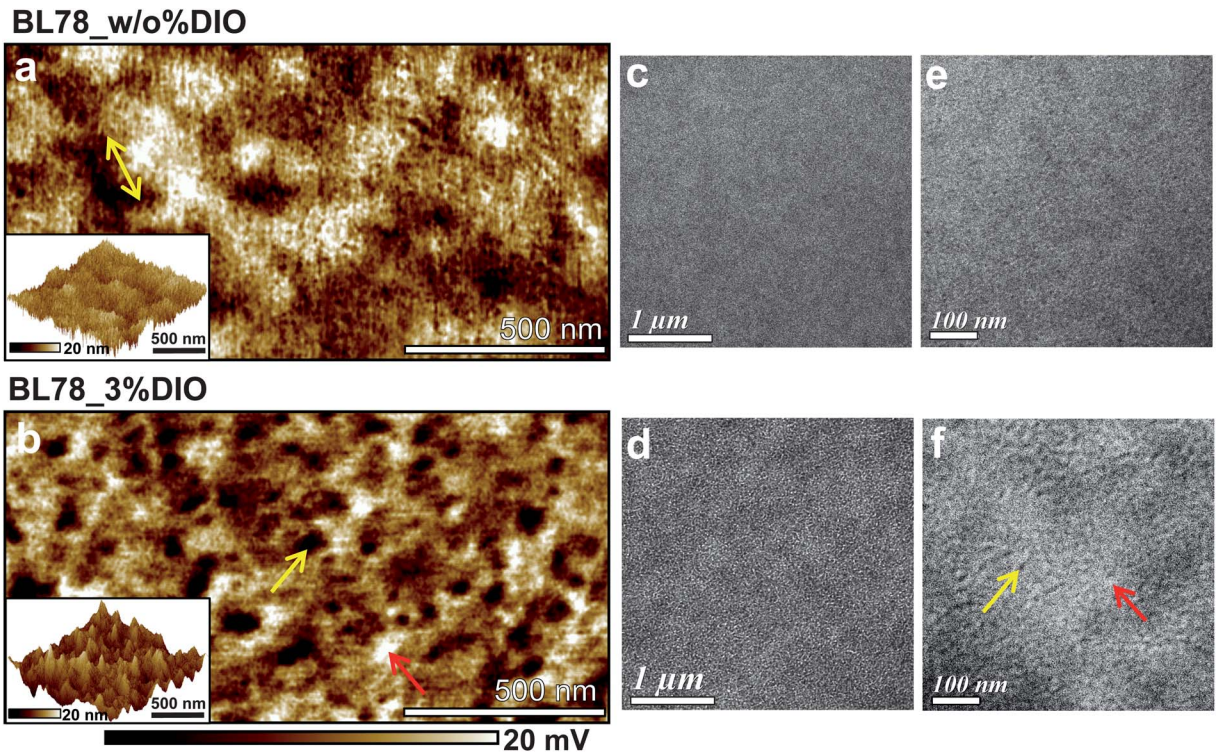

Fig. 3 (a and b) KPFM images of blend films of BL78_w/o DIO (a) and BL78_3% DIO (b) respectively. (c, d, e and f) TEM images of blend thin films of BL78_w/o DIO (c and e) and BL78_3% DIO (d and f) respectively. The indicated darker region by yellow arrow in (a) represents the PCBM fractal-aggregated network with fractal dimension $D_{PCBM} \sim 1.5$. The indicated brighter regions (red arrow) and darker regions (yellow arrow) in both (b) and (f) represent the phase-separated PCPDTBT and PCBM domains respectively. The insets of (a) and (b) show the topography images obtained from tapping mode AFM.

performed for D–A copolymer/fullerene BHJ for the first time in the present work. Fig. 3a and b show the KPFM images of BL78_w/o DIO and BL78_3% DIO blend films respectively with the AFM images shown in inset. The AFM image of BL78_w/o DIO film reveals a smooth surface topography while the BL78_3% DIO are much rougher with regions of tens of nanometers. This observation is consistent with that of ref. 9 however is difficult to identify each constitutes in either higher or lower topographic regions. For the KPFM images, the BL78_w/o DIO (Fig. 3a) exhibit the uniformly dispersed PCBM (dark color, low surface potential) which forms the meso-scale domains of hundreds of nanometers (yellow arrow indicated). On the other hand, the BL78_3% DIO (Fig. 3b) shows phase-separated domains of PCPDTBT (bright color, red indicated) and PCBM (dark color, yellow indicated) which reveal more remarkable surface potential contrasts as compared to the meso-scale domains in BL78_w/o% DIO. It is noteworthy that the KPFM tip we used is an n-type silicon cantilever coated with chromium, as a buffering layer, and a platinum–iridium5 alloy, as a conductive layer. The curvature radius of the tip is around 25 nm. Hence, the lateral resolution of the KPFM is around 50–60 nm at best. Nevertheless, the qualitative observation from KPFM images can still support the results of GISAXS analysis that the PCBM aggregation in BL78_w/o% DIO film is loose (pear-string-like) and open ($D_{\mathrm{PCBM}} \sim 1.5$) in comparison with the dense aggregation state with D_{PCBM} close to 3 in the BL78_3% DIO film. Similarly, the TEM observations in Fig. 3c and e of BL78_w/o DIO show dispersed distribution of PCBM and PCPDTBT with poor contrasts while Fig. 3d and f of BL78_3% DIO blend film reveal remarkable PCBM cluster domains (dark color) and aggregation domain/network of PCPDTBT crystals (bright color). Specifically, the TEM observation (low magnification) for the PCPDTBT crystal in the BL78_3% DIO blend film shows the short fibril-like or pear-string-like (aggregated by particles) structure (bright color in Fig. 3d). However, the high-magnification TEM image (Fig. 3f) is close to the fractal-like network domain as determined by GISAXS. The PCBM clusters seem to grow or exist around the PCPDTBT crystallites, suggesting the spatial interactions between them during the film formation process. Such a spatial distribution of PCBM clusters enhances the visually pear-string-like effect of PCPDTBT crystalline structure at the low magnification TEM observation.

Based on the above GISAXS, GIWAXS, TEM and KPFM studies, the schematic representations of the bi-hierarchical structures of PCPDTBT and PCBM phases in the blend films processed without and with DIO are shown in Fig. 4a and b, respectively. We interpret the mechanism of structural evolution of the blend films from a kinetic point of view. When the DIO is not present or few (≤0.5%), the PCBM phase is of a line-like fractal network (nearly dispersed). This structure is able to effectively disrupt the nucleation of PCPDTBT crystals or inhibit the crystallization as evidenced by the diffraction patterns of GIWAXS (Fig. 2b). Upon increasing the DIO more than 3%, the enough additive would

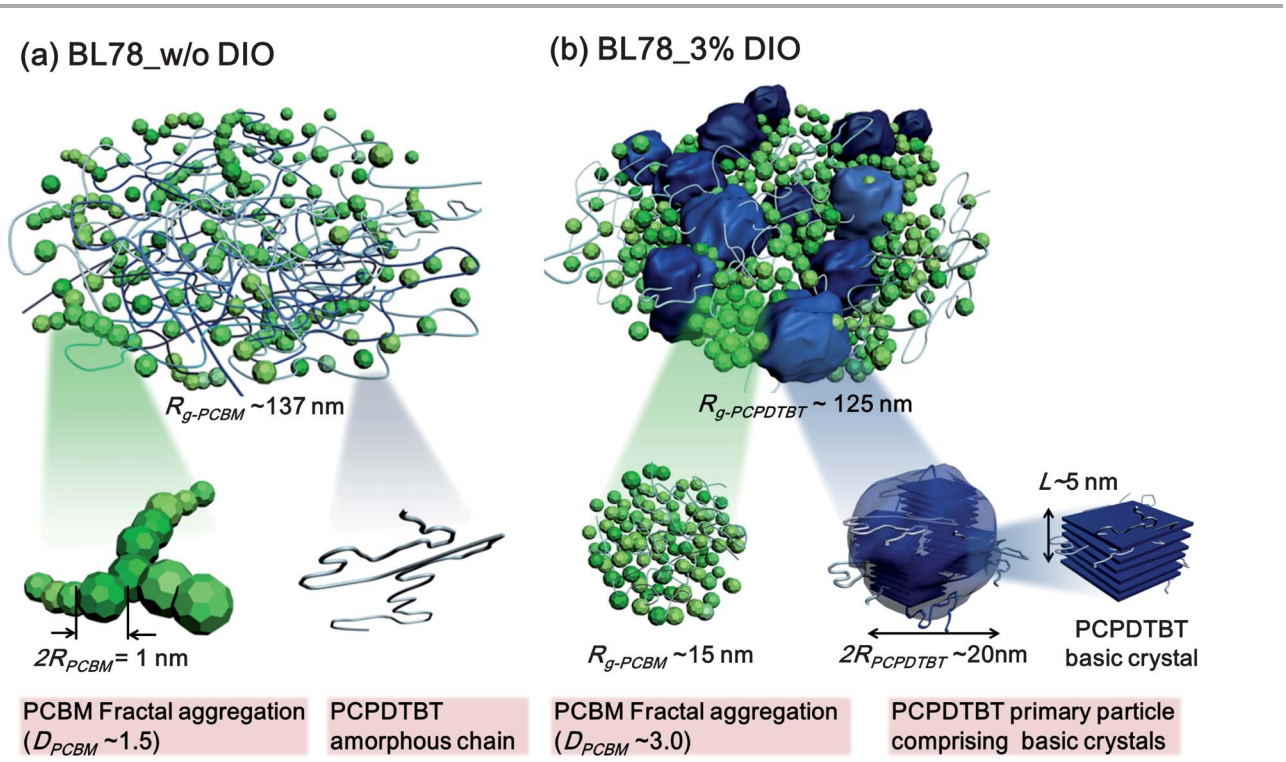

Fig. 4 Schematic diagrams of 3-D nanostructures of PCPDTBT/PCBM blend films processed (a) without DIO, *i.e.* BL78_w/o DIO and (b) with 3% DIO, *i.e.* BL78_3% DIO. The BL78_w/o DIO consists of PCPDTBT amorphous chains and PCBM fractal aggregation ($R_{g\text{-}PCBM} \sim 137$ nm, $D_{PCBM} \sim 1.5$) with PCBM molecule as the primary particle ($2R_{PCBM} \sim 1$ nm). The BL78_3% DIO films includes PCBM fractal aggregation ($R_{g\text{-}PCBM} \sim 15$ nm, $D_{PCBM} \sim 3.0$) and PCPDTBT fractal aggregation ($R_{g\text{-}PCPDTBT} \sim 125$ nm, $D_{PCPDTBT} \sim 3.0$) that is formed by PCPDTBT primary particles ($2R_{PCPDTBT} \sim 20$ nm) which comprise PCPDTBT basic crystals ($L \sim 5$ nm).

selectively dissolve the PCBM which remains in dispersed solution phase (during drying) longer than the PCPDTBT because the DIO has higher boiling point than the host solvent.[9] Therefore, PCPDTBT crystalline networks can naturally develop with faster kinetic growth analogous to the pristine polymers. The PCBM thus aggregates into domains surrounding polymer networks that formed earlier.

3.3 Comparison of morphologies of different BHJ blends affected by processing additive

We further try to clarify the discrepant observations of fullerene domain evolution among reported literatures.[3,8–12,15] Although the references used different solvent additives and polymers, they all fulfilled the criteria of controlling the BHJ morphology through additives, *i.e.* (1) the additive must have higher boiling point than the host solvent and (2) the BHJ blend must have selective solubility of one component than the other. The proposed mechanism in the present work is on the basis of the above guidelines. The PCPDTBT is a low crystallinity alternating D–A copolymer and hence the crystallization is almost completely inhibited by the loaded PCBM[6,7] in the blend (Fig. 3). The evolution from loosely and uniformly dispersed PCBM network in PCPDTBT amorphous matrix to dense aggregated PCBM domains implies the larger PCBM clusters when processing with additives[8,9,15] (Fig. 4). However, in the other cases of different D–A copolymer/fullerene BHJ,[3,10–12] the conjugated copolymers have higher crystallinity. When processing without additives, the loaded fullerene would not completely inhibit polymer crystallization and instead smaller aggregated domains still form. These smaller domains form earlier (faster kinetics) and subsequently confine fullerene in a large grainy space. Consequently, this leads to the microscopic observation of large-scale (hundreds of nanometer) fullerene grainy domains.[3,10–12] When processed with additives, the drying rate of fullerene furthermore slows down and the polymer crystallinity is enhanced, *i.e.* larger polymer aggregated domains form which leads to the smaller confined space for subsequent fullerene aggregation. We speculate the resultant size levels of hierarchical structures of both fullerene and polymer phases are similar to those of the PCPDTBT case. In this case the microscopic observations hence conclude an opposite evolution from large-scale fullerene domains to much smaller fullerene clusters when processing with DIO.[3,10–12] Therefore, the different observations among literatures are resulted from the different sizes of fullerene aggregates processed without additives as schemed in ESI, Fig. S9.† The film forming mechanism of the additive effect mentioned above can actually be applied to both cases. The interaction between additive molecules, fullerene and polymer during solvent evaporation is further proposed in the present work according to the resolved nanostructures and schemed in the ESI, Fig. S10.†

3.4 Morphology–performance correlation of PCPDTBT/PCBM blends affected by processing additive

The quantitatively resolved hierarchical nanostructures strongly affect the solar cell performances. The bi-continuous pathway formed by the respective hierarchical structures of PCPDTBT and PCBM enhances the exciton dissociation and free carrier transport. Fig. S11† plots the photocurrent–voltage curves of the photovoltaic devices based on different BHJs and the PCE and photovoltaic characteristics are summarized in Table S3.† The PCEs were improved by 45–55% from 3.2% to 5.2% and 4.9% after processing with 3% and 5% DIO respectively. Further increasing the DIO to 10% decreases the PCE. This can be attributed to the substantially residual additive solvent in the blend film gradually evaporates after casting, leading to the micron-scale segregation and thus non-uniform BHJ film as shown in Fig. S12.† The significantly improved PCEs with 3–5% DIO are correlated to the hierarchical nanostructures regarding to light harvesting, exciton dissociation and carrier transport. For the light harvesting, the absorption spectra shown in Fig. S13† enhance, red shift, and reveal a pronounced shoulder at 810 nm when processed with DIO. These results are attributed to the aggregated PCPDTBT crystallites domains in the DIO-processed (>3%) BHJ films which have longer conjugated length of π electrons, lower optical band gap and more π–π stacking interaction as compared to amorphous PCPDTBT chains in BL78_w/o DIO or BL78_0.5% DIO films. The narrowed optical band gap due to crystallization also accounts for the decreasing open circuit voltage (from 0.67 to 0.61 volts) with increasing DIO contents because of the upward shift of PCPDTBT highest occupied molecular orbital (HOMO) energy level, *i.e.* smaller energy difference between the HOMO of PCPDTBT and lowest unoccupied molecular orbital (LUMO) of PCBM. Considering the exciton dissociation, the structure of loose and open PCBM network dispersed in PCPDTBT of BL78_w/o DIO is expected to provide substantially large interface area for exciton dissociation. However, though a large amount of electrons inject into PCBM upon illumination, the discontinuous pathways (in molecular scale inter-dispersion) would result in insufficient separated distance between electrons and holes and thus considerable geminate recombination (a loss that decreases the yield of useful carriers) occurs due to electrostatic attraction.[31] On the other hand, the DIO-processed BHJ reveals bi-continuous routes of a dense fractal-aggregated PCPDTBT network (formed by ~20 nm PCPDTBT primary particles) and surrounded PCBM fractal aggregations ($R_{g\text{-PCBM}} \sim$ 15 nm). These continuous pathways enable the dissociated free electrons and holes to efficiently escape from geminate recombination and move apart. The reduction of geminate recombination from 50% to 30% when processing with additives has been recently reported[32] which is consistently correlated to our nanostructures. Furthermore, though the interfaces between PCPDTBT and PCBM are reduced when processing with DIO, the domain size of PCPDTBT aggregated crystallites around 20 nm can still ensure excitons to encounter interfaces and dissociation before recombination (the diffusion length of exciton ~10 nm in conducting polymer).[33] Finally, subsequent to carrier dissociation, the free carrier transport toward the electrode through the inter-connected fractal-aggregated domains is apparently more efficient as compared to that of molecular scale dispersion when processing without DIO. The mobility improvements shown in Fig. S14 and Table S4† when

processing with DIO for both electrons and holes provides the evidences, *i.e.* μ_e: from 2.3×10^{-5} cm^2 V^{-1} s^{-1} to 3.8×10^{-4} cm^2 V^{-1} s^{-1}; μ_h: from 1.4×10^{-5} cm^2 V^{-1} s^{-1} to 2.6×10^{-5} cm^2 V^{-1} s^{-1} where μ_e and μ_h are electron and hole mobility respectively. Interestingly, the hole mobility is doubled due to the fractal-aggregated network of PCPDTBT crystallites. The electron mobility is much more significantly improved by an order that is resulted from the structures of inter-connected aggregated PCBM clusters. In short, the bi-continuous phase of PCPDTBT and PCBM formed by the respective hierarchical nanostructures tuned by additives is the most important factor for achieving both high efficient exciton dissociation and carrier transport. The continuous PCBM phases are particularly critical and dominate the device performances.

3.5 Morphologies of PCPDTBT/PCBM blends affected by the blending ratio

The effect of the PCBM amount on the nanomorphology of blend films processed with 3% DIO was investigated. Fig. 2c and d show the GISAXS and GIWAXS profiles of the blend films containing 33%, 50% and 78% (in weight) of PCBM (denoted as BL33_3% DIO, BL50_3% DIO and BL78_3% DIO), respectively. As compared to the GISAXS profile of P_3% DIO, the variation of GISAXS profiles for these blend films with the PCBM content is remarkable in the low- and middle-Q regions. It suggests the structure of crystalline polymer network influenced by the PCBM is significantly different from that in the P_3% DIO. Eqn (4) for the bi-fractal (hierarchical) structures from PCBM and PCPDTBT structures can be used to fit well the measured GISAXS intensities (solid lines in Fig. 2c). The structural parameters determined by GISAXS analysis is also listed in Table 2. The relative volume fraction of PCPDTBT network structure is found to decrease with increasing PCBM content which is consistently observed in the decreasing intensities of (100) scattering peaks in GIWAXS profiles (Fig. 2d). Apparently, the loading of PCBM considerably interrupts the crystallization of PCPDTBT as we have mentioned. On the other hands, for the PCBM phase the relative volume fraction of fractal structure significantly increases from 13% to 34% when increasing the PCBM content up to 78% with aggregated size ~15 nm. The corresponding PCEs exhibit significant improvements from 1.9% to 5.2% when the PCBM content reaches 78% as listed in Table 2. The photocurrent–voltage plots and photovoltaic characteristics are summarized in the ESI, Fig. S15 and Table S5 respectively.†

It is noteworthy that the optimized PCBM content in D–A copolymer/PCBM BHJs (50–60%)[1–5] is typically higher than that of conventional P3HT system (40–50%).[15,17] PCPDTBT/PCBM system has particularly higher (~78%) optimized PCBM content.[8,9] The bi-hierarchical nanostructures as well as the kinetics during film forming still play the critical roles. The device PCE is dominantly affected by the continuous PCBM phase according to the correlation between the hierarchical nanostructures and optoelectronic properties (ESI, Fig. S11–S14 and Table S3 and S4†). The PCPDTBT copolymer has naturally lower crystallinity as compared to other conducting polymers and thus the earlier formed PCPDTBT aggregated domains leaves more space for subsequent PCBM aggregation. As a result, substantial amount of PCBM is required to aggregate into the space left by PCPDTBT and construct continuous phases for efficient carrier transport. This reasonably explains the typically trend that the optimized content of fullerene increases with decreasing crystallinity of conjugated polymers. The results can serve as a rational guide in optimizing the device processing and associated synthesis of alternating D–A copolymer.

Conclusions

In summary, the PCPDTBT/PCBM BHJ reveals distinctive bi-hierarchical nanostructures for both PCPDTBT and PCBM. The fractal aggregated domains/networks in terms of inter-dispersion or inter-confinement between PCPDTBT and PCBM tuned by solvent additives and PCBM contents were quantitatively resolved. Both processing effects were clearly identified and correlated to the photovoltaic properties through the resolved nanostructural evolution. The film forming mechanism is hence rationally proposed and used to coordinate and clarify the currently reported literatures regarding the structural characterization and processing optimization of different D–A copolymer/fullerene BHJ solar cells. The present work significantly extends the current knowledge of the interaction among bi-hierarchical nanostructures, solvent additive effect, fullerene content effect, film forming mechanism and nanostructural evolution of D–A copolymer/fullerene BHJ solar cells.

Acknowledgements

Financial supports for this work obtained from the National Science Council of Taiwan (NSC 101-3113-E-002-010 and NSC 101-2120-M-002-003) and the Institute of Nuclear Energy Research (Projects 1022001INER025) are highly appreciated.

Notes and references

1 H. J. Son, W. Wang, T. Xu, Y. Liang, Y. Wu, G. Li and L. Yu, *J. Am. Chem. Soc.*, 2011, **133**, 1885.
2 H.-Y. Chen, J. Hou, S. Zhang, Y. Liang, G. Yang, Y. Yang, L. Yu, Y. Wu and G. Li, *Nat. Photonics*, 2009, **3**, 649.
3 Y. Liang, Z. Xu, J. Xia, S.-T. Tsai, Y. Wu, G. Li, C. Ray and L. Yu, *Adv. Mater.*, 2010, **22**, E135.
4 S. C. Price, A. C. Stuart, L. Yang, H. Zhou and W. You, *J. Am. Chem. Soc.*, 2011, **133**, 4625.
5 L. Dou, J. You, J. Yang, C.-C. Chen, Y. He, S. Murase, T. Moriarty, K. Emery, G. Li and Y. Yang, *Nat. Photonics*, 2012, **6**, 180.
6 J. T. Rogers, K. Schimdt, M. F. Toney, G. C. Bazan and E. J. Kramer, *J. Am. Chem. Soc.*, 2012, **134**, 2884.
7 J. T. Rogers, K. Schimdt, M. F. Toney, E. J. Kramer and G. C. Bazan, *Adv. Mater.*, 2011, **23**, 2284.
8 J. Peet, J. Y. Kim, N. E. Coates, W.-L. Ma, D. Moses, A. J. Heeger and G. C. Bazan, *Nat. Mater.*, 2007, **6**, 497.

9 J. K. Lee, W. L. Ma, C. J. Brabec, J. Yuen, J. S. Moon, J. Y. Kim, K. Lee, G. C. Bazan and A. J. Heeger, *J. Am. Chem. Soc.*, 2008, **130**, 3619.

10 J. S. Moon, C. J. Takacs, S. Cho, R. C. Coffin, H. Kim, G. C. Bazan and A. J. Heeger, *Nano Lett.*, 2010, **10**, 4005.

11 M.-S. Su, C.-Y. Kuo, M.-C. Yuan, U.-S. Jeng, C.-J. Su and K.-H. Wei, *Adv. Mater.*, 2011, **23**, 3315.

12 S. J. Lou, J. M. Szarko, T. Xu, L. Yu, T. J. Marks and L. X. Chen, *J. Am. Chem. Soc.*, 2011, **133**, 20661.

13 W. Chen, M. P. Nikiforov and S. B. Darling, *Energy Environ. Sci.*, 2012, **5**, 8045.

14 J. Rivnay, S. C. B. Mannsfeld, C. E. Miller, A. Salleo and M. F. Toney, *Chem. Rev.*, 2012, **112**, 5488.

15 Y. Gu, C. Wang and T. P. Russel, *Adv. Energy Mater.*, 2012, **6**, 683.

16 F. Liu, Y. Gu, C. Wang, W. Zhao, D. Chen, A. L. Briseno and T. P. Russell, *Adv. Mater.*, 2012, **24**, 3947.

17 H.-C. Liao, C.-S. Tsao, T.-H. Lin, M.-H. Jao, C.-M. Chuang, S.-Y. Chang, Y.-C. Huang, Y.-T. Shao, C.-Y. Chen, C.-J. Su, U.-S. Jeng, Y.-F. Chen and W.-F. Su, *ACS Nano*, 2012, **6**, 1657.

18 H.-C. Liao, C.-S. Tsao, T.-H. Lin, C.-M. Chuang, C.-Y. Chen, U.-S. Jeng, C.-H. Su, Y.-F. Chen and W.-F. Su, *J. Am. Chem. Soc.*, 2011, **133**, 13064.

19 W.-R. Wu, U.-S. Jeng, C.-J. Su, K.-H. Wei, M.-S. Su, M.-Y. Chiu, C.-Y. Chen, W.-B. Su, C.-H. Su and A.-C. Su, *ACS Nano*, 2011, **5**, 6233.

20 J. W. Kiel, A. P. R. Eberle and M. E. Mackay, *Phys. Rev. Lett.*, 2010, **105**, 167801.

21 W. Chen, T. Xu, F. He, W. Wang, C. Wang, J. Strzalka, Y. Liu, J. Wen, D. J. Miller, J. Chen, K. Hong, L. Yu and S. B. Darling, *Nano Lett.*, 2011, **11**, 3707.

22 Y. He, H.-Y. Chen, J. Hou and Y. Li, *J. Am. Chem. Soc.*, 2010, **132**, 1377.

23 M. Lenes, G.-J. A. H. Wetzelaer, F. B. Kooistra, S. C. Veenstra, J. C. Hummelen and P. W. Blom, *Adv. Mater.*, 2008, **20**, 2116.

24 J. L. Baker, L. H. Jimison, S. Mannsfeld, S. Volkman, S. Yin, V. Subramanian, A. Salleo, A. P. Alivisatos and M. F. Toney, *Langmuir*, 2010, **26**, 9146.

25 U. Jeng, C.-H. Su, C.-J. Su, K.-F. Liao, W.-T. Chuang, Y.-H. Lai, Y.-J. Chang, Y.-J. Chen, Y.-S. Huang, M.-T. Lee, K.-L. Yu, J.-M. Lin, D.-G. Liu, C.-F. Chang, C.-Y. Liu, C.-H. Chang and K.-S. Liang, *J. Appl. Crystallogr.*, 2010, **43**, 110.

26 P. Debye, R. Anderson and H. Brumberger, *J. Appl. Phys.*, 1957, **28**, 679.

27 R. Zhang, B. Li, M. C. Iovu, M. Jeffries-EL, G. Sauve, J. Cooper, S. J. Jia, S. Tristram-Nagle, D. M. Smilgies, D. N. Lambeth, R. D. McCullough and T. Kowalewski, *J. Am. Chem. Soc.*, 2006, **11**, 3480.

28 B. A. Collins, J. R. Tumbleston and H. Ade, *J. Phys. Chem. Lett.*, 2011, **2**, 3135.

29 S. R. J. Kline, *J. Appl. Crystallogr.*, 2006, **39**, 895.

30 J. Teixeira, *J. Appl. Crystallogr.*, 1988, **21**, 781.

31 S. K. Pal, T. Kesti, M. Maiti, F. Zhang, O. Inganas, S. Hellstrom, M. R. Andersson, F. Oswald, F. Langa, T. Osterman, T. Pascher, A. Yartsev and V. Sundstrom, *J. Am. Chem. Soc.*, 2010, **132**, 12440.

32 F. Etzold, I. A. Howard, N. Forler, D. M. Cho, M. Meister, H. Mangold, J. Shu, M. R. Hansen, K. Mullen and F. Laquai, *J. Am. Chem. Soc.*, 2012, **134**, 10569.

33 O. V. Mikhnenko, H. Azimi, M. Scharber, M. Morana, P. W. M. Blom and M. A. Loi, *Energy Environ. Sci.*, 2012, **5**, 6960.